IMMUNOLOGY

KDM6B drives epigenetic reprogramming associated with lymphoid stromal cell early commitment and immune properties

Marvin Sylvestre[1]†, Nicolas Barbier[1]†, Vonick Sibut[1], Saba Nayar[2], Céline Monvoisin[1], Simon Leonard[1,3], Julien Saint-Vanne[1,4], Ansie Martin[1], Marion Guirriec[1], Maëlle Latour[4], Florence Jouan[1], Sylvain Baulande[5], Mylène Bohec[5], Léa Verdière[1], Fatima Mechta-Grigoriou[6], Frédéric Mourcin[1], Nicolas Bertheuil[1,7], Francesca Barone[8], Karin Tarte[1,4]‡*, David Roulois[1]‡*

Mature lymphoid stromal cells (LSCs) are key organizers of immune responses within secondary lymphoid organs. Similarly, inflammation-driven tertiary lymphoid structures depend on immunofibroblasts producing lymphoid cytokines and chemokines. Recent studies have explored the origin and heterogeneity of LSC/immunofibroblasts, yet the molecular and epigenetic mechanisms involved in their commitment are still unknown. This study explored the transcriptomic and epigenetic reprogramming underlying LSC/immunofibroblast commitment. We identified the induction of lysine demethylase 6B (KDM6B) as the primary epigenetic driver of early immunofibroblast differentiation. In addition, we observed an enrichment for KDM6B gene signature in murine inflammatory fibroblasts and pathogenic stroma of patients with autoimmune diseases. Last, KDM6B was required for the acquisition of LSC/immunofibroblast functional properties, including the up-regulation of CCL2 and the resulting recruitment of monocytes. Overall, our results reveal epigenetic mechanisms that participate in the early commitment and immune properties of immunofibroblasts and support the use of epigenetic modifiers as fibroblast-targeting strategies in chronic inflammation.

INTRODUCTION

Lymphoid stromal cells (LSCs) refer to a heterogeneous cell compartment within secondary lymphoid organs, consisting of two main specialized cell networks expressing gp38/podoplanin (PDPN) (*1*): PDPN$^+$CCL19$^+$CCL21$^+$ extrafollicular fibroblastic reticular cells (FRCs), and PDPN$^+$CD21$^+$CD35$^+$ follicular dendritic cells (FDCs) populating B cell follicles. Single-cell RNA sequencing (scRNAseq) and imaging studies highlight additional levels of heterogeneity in murine and human LSCs, outlining numerous subsets of FRCs linked to various localizations and functions, as well as two subsets of FDCs, reflecting their sublocalization within the germinal center (*2*–*7*). During embryogenesis, LSCs originate from mesenchymal lymphoid tissue organizers (mLTo) under the control of the nuclear factor κB (NF-κB) pathway. In particular, lymphoid tissue inducers produce lymphotoxin α1β2 (LT), thereby activating LTβR-expressing mLTo (*8*). In adults, LSCs derive from local resident mesenchymal precursors, including perivascular cells and adipocyte precursors, and require both tumor necrosis factor–α (TNF) and LT, produced by immune cells, for their maturation and maintenance as immunologically competent cells (*9*, *10*). Although elegant cell-fate mapping approaches and cell trajectory reconstructions based on scRNAseq analyzes have suggested cell specification pathways for LSC subsets, the underlying molecular mechanisms remain largely underexplored.

Chronic inflammatory conditions, such as infections, autoimmune diseases, and cancers, are associated with the development of pathogenic ectopic tertiary lymphoid structures (TLSs) in peripheral tissues (*11*). TLSs are made up of immune cells, including lymphocytes and myeloid cells, endothelial cells, and PDPN$^+$ stromal cells with LSC-like features called immunofibroblasts (*12*, *13*). Immunofibroblasts support the recruitment, organization, and maintenance of TLS immune cells that in turn contribute to their dynamic plasticity. Early activation of local immunofibroblast progenitors relies on inflammatory factors released by resident cells and recruited monocyte-derived macrophages, while the further expansion of the fibroblast network and the organization of TLS involve cross-talk with T and B cells (*13*–*16*). In human, adipose-derived stromal cells (ASCs) are specifically prone to interact with immune cells compared to their bone marrow counterpart (*17*). Moreover, ASCs could be efficiently committed toward LSC/immunofibroblast-like cells in vitro (*18*), making them an attractive cell model to capture the driving mechanisms of LSC/immunofibroblast commitment.

Epigenetic modifications, such as DNA methylation and histone modifications, affect the chromatin structure, altering its accessibility to transcription factors (TFs) and other gene regulators (*19*, *20*). EZH2 is a component of the polycomb repressive complex 2 responsible for the trimethylation of H3K27. This favors adipogenic

[1]Honeycomb team, Equipe Labellisée par la Ligue Nationale Contre le Cancer, Univ Rennes, INSERM, EFS, UMR S1236, Rennes, France. [2]Centre for Translational inflammation Research, Institute of Inflammation and Ageing, College of Medical and Dental Sciences, University of Birmingham Research Laboratories, Queen Elizabeth Hospital, Birmingham, UK. [3]LabEx IGO "Immunotherapy, Graft, Oncology", F-35043 Nantes, France. [4]SITI, Pôle Biologie, CHU Rennes, F-35033 Rennes, France. [5]Institut Curie Genomics of Excellence (ICGex) Platform, Institut Curie Research Center, PSL Research University, F-75005 Paris, France. [6]Stress and Cancer Laboratory, Equipe Labellisée par la Ligue Nationale Contre le Cancer, Institut Curie, INSERM, U830, PSL Research University, 26, rue d'Ulm, F-75005 Paris, France. [7]Department of Plastic Surgery, CHU Rennes, F-35033 Rennes, France. [8]Candel Therapeutics, Needham, MA, USA.
*Corresponding author. Email: karin.tarte@univ-rennes.fr (K.T.); david.roulois@univ-rennes.fr (D.R.)
†These authors contributed equally to this work.
‡These authors contributed equally to this work.

and inhibits osteogenic differentiation potential of bone marrow–mesenchymal stromal cells (BM-MSCs). Conversely, the H3K27me3 demethylases, lysine demethylase 6A (KDM6A) (also known as UTX) and lysine demethylase 6B (KDM6B) (JMJD3) inhibit adipogenesis and promote osteogenesis, suggesting a key role for H3K27-centered epigenetic switch in stromal cell fate specification (*21*–*24*). KDM6B is widely known for its role during inflammatory response and harbors NF-κB binding sites in its promoter (*25*, *26*). KDM6B is up-regulated during respiratory syncytial virus infection, and its inhibition results in a decreased production of CCL2 and CCL5 chemokines (*27*). KDM6B also contributes to the transforming growth factor–β–dependent activation of cutaneous fibroblasts in systemic sclerosis through the removal of the repressive mark H3K27me3 at the promoter of *FRA2* (*28*). Last, KDM6B inhibition in fibroblast-like synoviocytes (FLSs) of rheumatoid arthritis (RA) prevents their proliferation, through the repression of *PCNA* (*29*). In line with this result, the sustained expression of inflammatory genes in RA FLS was recently linked to prolonged TNF-induced epigenetic modifications, including persistent deposit of the activating mark H3K27ac (*30*). Together, these data highlight the crucial role of H3K27 modifications in stromal cell differentiation and activation and raise the question of their impact on LSC/immunofibroblast early commitment and function.

The current study combined an in vitro model of human ASC commitment into LSC/immunofibroblast-like cells and an in vivo model of murine TLS induction. In both cases, the differentiation of LSC/immunofibroblasts was associated with a specific and early NF-κB–dependent induction of KDM6B, which could bind directly to LSC genes. We then defined a KDM6-specific gene signature that was found to be enriched in murine inflammatory fibroblasts and in human pathogenic immunofibroblasts from patients with autoimmune disease. Moreover, we demonstrated, using a KDM6 inhibitor, that KDM6B was required for the acquisition of LSC/immunofibroblast phenotype and functions, including up-regulation of CCL2 production and resulting recruitment of monocytes. Together, our results shed light on epigenetic mechanisms involved in LSC commitment and function.

RESULTS

TNF/LT triggers in vitro differentiation of stromal precursors into immunofibroblasts

To dissect the molecular mechanisms of immunofibroblast differentiation, we previously developed an in vitro model of human ASC-to-immunofibroblast commitment under a combination of TNF and LT (*18*, *31*) (Fig. 1A). We first investigated the early molecular makeup of in vitro–induced immunofibroblasts by analyzing their gene expression profile (GEP) after 6 hours (H6) of TNF/LT stimulation ($n = 4$). RNA sequencing (RNA-seq) analysis identified 256 up-regulated and 97 down-regulated genes at H6 (adjusted $P < 0.01$, fold change >2, DESeq 2 analysis) compared to unstimulated ASC (Fig. 1B and table S1). Up-regulated genes belonged to immunomodulatory chemokines and cytokines (*CCL2*, *CCL5*, *CXCL10*, *IL1B*, and *IL8*), and adhesion molecules (*PDPN*, *ICAM1*, *TNFRSF9*, and *VCAM1*), classically associated with immunofibroblast phenotype (Fig. 1C). We next defined immunofibroblast signature by analyzing the GEP of ASC stimulated for 3 days (D3) by TNF/LT, highlighting 966 up-regulated and 899 down-regulated genes (adjusted $P < 0.01$, fold change >2, DESeq 2 analysis; Fig. 1D and table S2). We used recently established gene signatures of $Pi16^+$ universal fibroblast precursors and $Ccl19^+$ FRC (*32*) to confirm that treating ASC by TNF/LT for D3 in vitro mimicked the commitment of stromal precursors into LSC/immunofibroblasts in vivo (Fig. 1E). Most of the 256 genes that were up-regulated at H6 remained up-regulated at D3 ($P = 1.38 \times 10^{-7}$, hypergeometric test) (fig. S1A). Pathway enrichment analysis of up-regulated genes at both H6 and D3 revealed an enrichment in NF-κB and cytokine/chemokine signaling pathways (fig. S1, B and C). This was further confirmed using gene set enrichment analysis, showing an enrichment in both inflammatory response and TNF signaling through NF-κB pathway at H6 and D3 (fig. S1D). In contrast, analysis of down-regulated genes at both H6 and D3 revealed a decrease of genes associated with commitment into other stromal lineages such as white fat cell differentiation and neural crest differentiation (fig. S1, E and F). To further validate that ASCs committed in vitro into immunofibroblasts displayed LSC features, we evaluated the relationship between the immunofibroblast signatures at H6 and D3 and the published GEP of human purified mature LSCs (FRCs and FDCs) (*33*). ASCs differentiated in vitro into early (D1) and mature (D21) adipocytes (*34*) were used as controls. We observed a positive correlation between in vitro immunofibroblasts and mature LSCs and a negative correlation between in vitro immunofibroblasts and D1 adipocytes (Pearson correlation, $^*P < 0.05$, $^{**}P < 0.01$, $^{***}P < 0.001$) (Fig. 1F). Together, these data highlight that TNF/LT treatment induces commitment of ASCs toward immunofibroblasts with LSC-like features.

Early KDM6B induction and binding is associated with immunofibroblast commitment

Given the previously described involvement of KDM6B in stromal cell differentiation and activation (*21*–*23*), we studied KDM regulation during stromal cell response to TNF/LT. Out of the 17 detectable KDMs, only *KDM6B* showed an increased expression, peaking at H2 after TNF/LT stimulation of human ASC (Fig. 2A). KDM6B up-regulation was restricted to TNF/LT and was not observed with other classical stroma inflammatory signals (*35*, *36*), such as Toll-like receptor activation by lipopolysaccharide (LPS) or Poly I:C, or interferon-γ (IFN-γ), as well as interleukin-17 (IL-17) stimulation (Fig. 2B). The efficient knockdown of *RELA* or *RELB*, both up-regulated upon TNF/LT treatment, impaired *KDM6B* induction without affecting *KDM6A* expression, underlying the relationship between NF-κB activation and KDM6B induction in response to TNF/LT treatment (fig. S2, A and B). We then validated that KDM6B could effectively bind lymphoid stroma genes by performing KDM6B CUT&RUN (*37*) analysis on ASCs and early immunofibroblasts (H6 after TNF/LT treatment). After peak calling, we identified differentially bounded regions between treated and untreated cells (gain of 2676 and loss of 856 regions, adjusted $P < 0.05$, fold change >2 or < −2, DESeq 2 analysis; Fig. 2C). Most of these differentially bounded regions were associated with an increase binding of KDM6B upon TNF/LT (75.8% versus 24.2%, $P < 0.0001$; fig. S2C). Kyoto Encyclopedia of Genes and Genomes (KEGG) pathway analysis of KDM6B-enriched genes highlighted NF-κB pathway and cytokine/chemokine-mediated pathways (Fig. 2D). Moreover, evaluation of TF motif enrichment using HOMER and TF target genes using the TRRUST database and EnrichR in KDM6B-enriched peaks at H6, identified

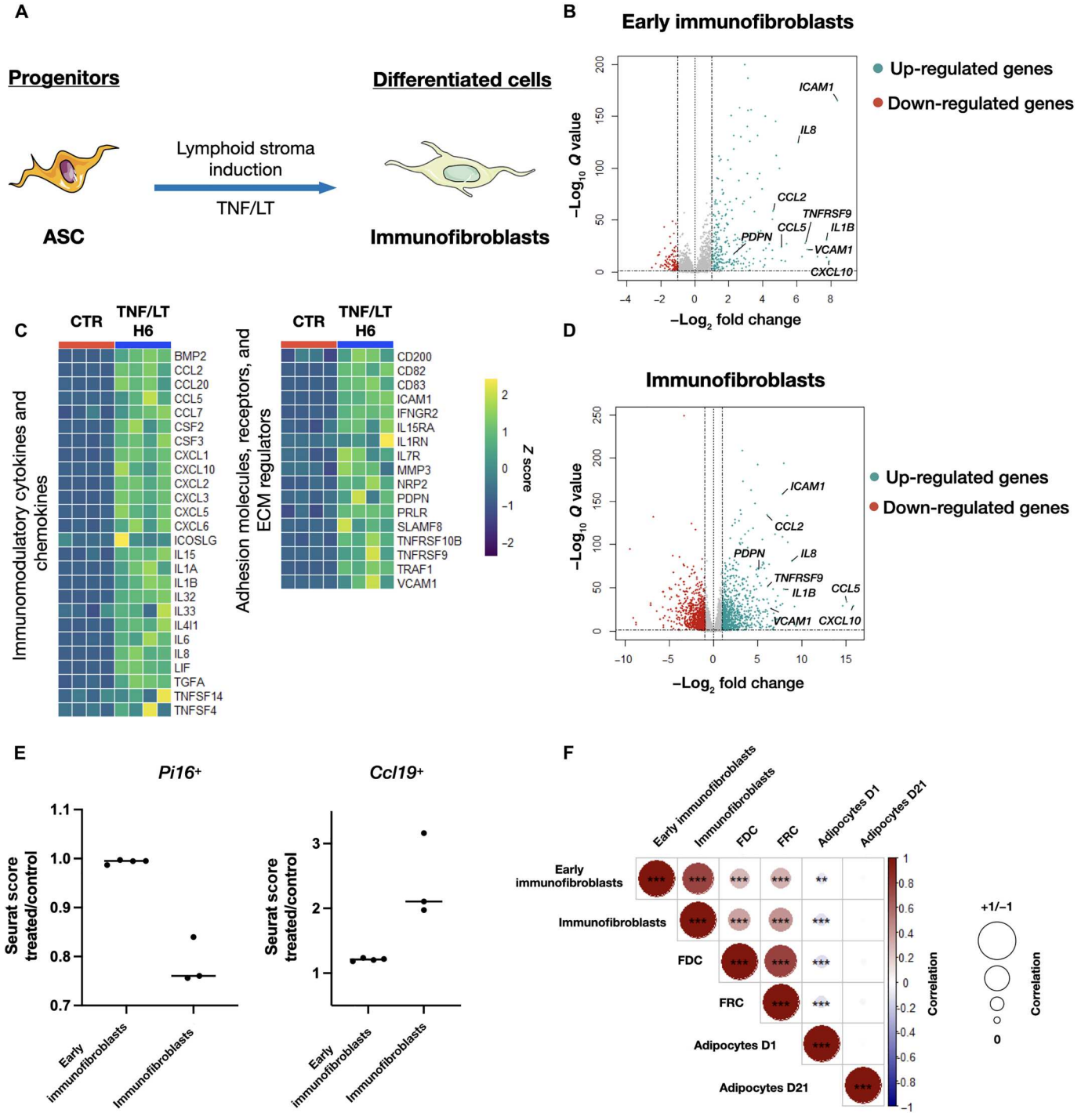

Fig. 1. Kinetic transcriptomic analysis of in vitro committed immunofibroblasts. (**A**) Representation of the in vitro model of adipose-derived stromal cell (ASC) to immunofibroblast commitment. (**B**) RNA sequencing (RNA-seq) analysis of ASC treated with tumor necrosis factor–α (TNF)/lymphotoxin α1β2 (LT) during 6 hours (H6) (early immunofibroblasts). Differentially expressed genes were represented through a volcano plot with up-regulated genes (adjusted $P < 0.05$, fold change >2) in blue, and down-regulated genes (adjusted $P < 0.05$, fold change < −2) in red, as identified by DESeq 2 analysis ($n = 4$). (**C**) Heatmap showing the normalized counts of selected immunomodulatory cytokines, chemokines, receptors, adhesion molecules, and ECM regulators upon ASC treatment with TNF/LT for H6 compared to untreated cells (CTR), mean value of four different experiments was visualized with *z* score through a color code. (**D**) RNA-seq analysis of ASC treated with TNF/LT during 3 days (D3) (immunofibroblasts). Differentially expressed genes were represented through a volcano plot with up-regulated genes (adjusted $P < 0.05$, fold change >2) in blue, and down-regulated genes (adjusted $P < 0.05$, fold change < −2) in red, as identified by DESeq 2 analysis ($n = 3$). (**E**) Seurat score enrichment analysis of the *Pi16*$^+$ fibroblast (left) and *Ccl19*$^+$ fibroblastic reticular cell (FRC) (right) gene signatures in early immunofibroblasts and immunofibroblasts at day 3 ($n = 4$ and $n = 3$, respectively). (**F**) Pearson correlation matrix was performed using up-regulated genes of H6 and D3 immunofibroblasts, native lymphoid stromal cell (LSC) signatures [FRC and follicular dendritic cell (FDC)], and signatures of adipocytes differentiated from ASC (D1 and D21). Size of the dots represents the absolute correlation value, and color code is associated with positive (red) or negative (blue) correlation. (*$P < 0.05$, **$P < 0.01$, ***$P < 0.001$.)

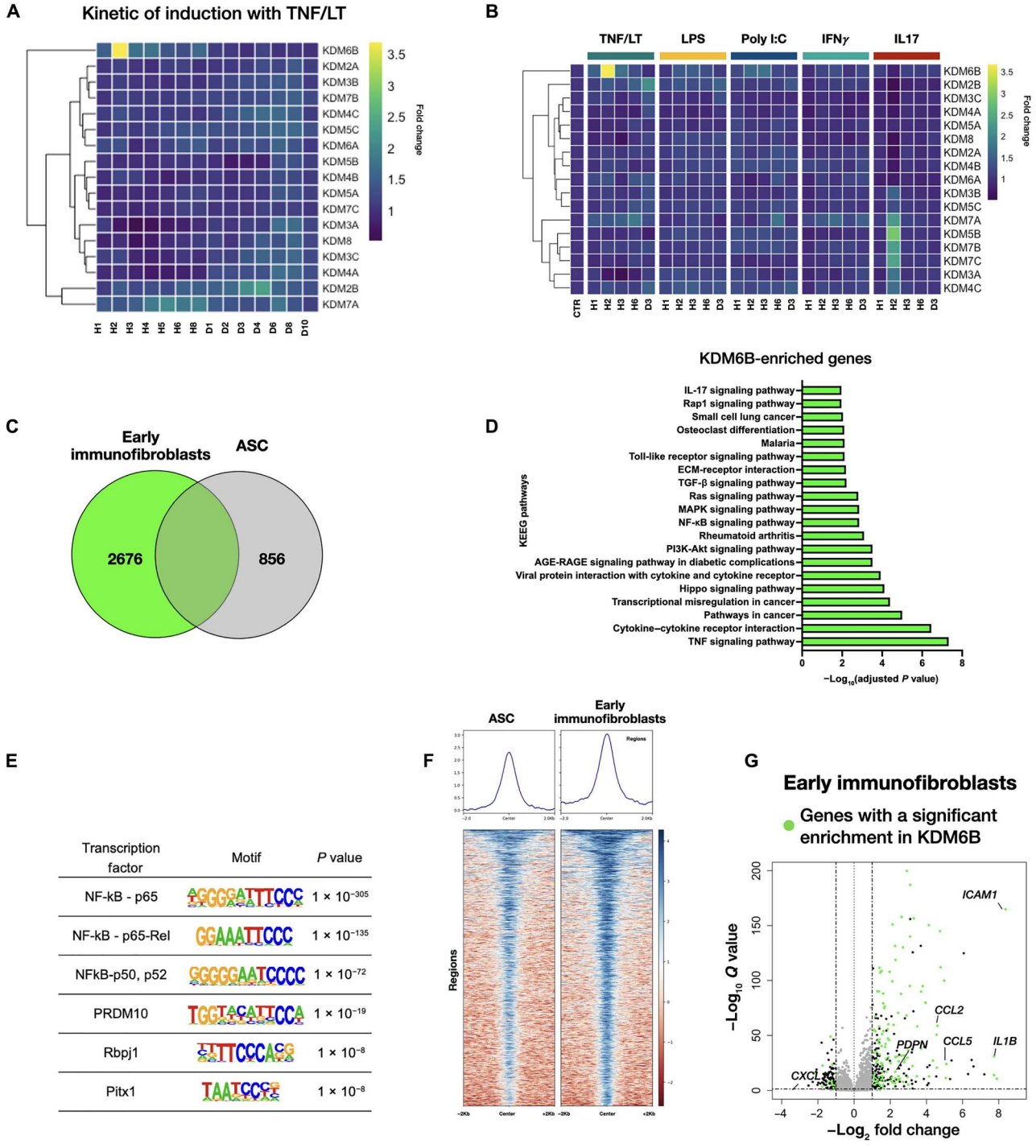

Fig. 2. Early KDM6B induction and binding is associated to immunofibroblast commitment. (**A**) Heatmap showing the mean expression (n = 3) of the 17 KDM detected in adipose-derived stromal cells (ASCs) treated with tumor necrosis factor–α (TNF)/lymphotoxin α1β2 (LT) for 1 hour (H1) to 10 days (D10). Expression data (n = 3) are normalized with H0 expression as a control, and mean value of fold change are represented according to the color code scale. (**B**) Heatmap showing the mean expression (n = 3) of the 17 KDM detected in ASCs treated with TNF/LT, lipopolysaccharide (LPS), Poly I:C, interferon-γ (IFN-γ), or interleukin-17 (IL-17) for H1 to 3 days (D3) (n = 3). Expression data are normalized with H0 expression as a control, and mean value of fold change are represented according to the color code scale. (**C**) Visualization of the KDM6B binding peaks in CTR (gray) or early immunofibroblasts (green). Differential repartition was assessed by a chi-square test with equal repartition defined as a null hypothesis ($P < 0.0001$). (**D**) The genes enriched for KDM6B binding in ASC treated by TNF/LT at H6 were analyzed by EnrichR using Kyoto Encyclopedia of Genes and Genomes (KEGG) pathway analysis. −LOG10(adjusted P value) of the top 20 enriched KEGG pathways were visualized through histograms. (**E**) Motif enrichment analysis at KDM6B enriched peaks in early immunofibroblasts (H6) as defined using HOMER. Only motifs with $P < 1 \times 10^{-4}$ were shown. (**F**) KDM6B density pileups and tag density heatmaps of KDM6B binding regions associated with genes induced in early immunofibroblasts (H6) were compared between ASCs (CTR) and early immunofibroblasts (H6) (−/+ 2-kb windows). (**G**) ASC were treated with TNF/LT during 6 hours (H6) and differentially expressed genes were represented through a volcano plot. Genes with a significative KDM6B enrichment at H6 after treatment were highlighted in green (adjusted $P < 0.05$, fold change >2, DESeq 2 analysis).

members of NF-κB family as key targets of KDM6B during LSC commitment (Fig. 2E and fig. S2D). Last, the genes up-regulated at H6 after TNF/LT treatment were enriched for KDM6B binding ($P = 5.5 \times 10^{-39}$, hypergeometric test), including *CCL2*, *CCL5*, *PDPN*, *ICAM1*, *CXCL10*, and *IL1B* (Fig. 2, F and G, and fig. S2, E to G). Together, these data demonstrate that TNF/LT combination triggers molecular reprogramming of ASCs into immunofibroblasts in association with NF-κB–dependent early induction of KDM6B.

GSK-J4 treatment partially impairs immunofibroblast commitment in vitro

To further evaluate the role of KDM6B during early immunofibroblast commitment, we stimulated ASCs by TNF/LT in the presence or not of the KDM6-specific inhibitor GSK-J4 and analyzed their GEP by RNA-seq at H6. Within genes up-regulated in early immunofibroblast, 72 were negatively affected by GSK-J4 treatment (adjusted $P < 0.05$, fold change >2, DESeq 2 analysis), including *CXCL10*, *VCAM1*, *TNFRSF9*, *PDPN*, *IL1B*, *CCL2*, and *CCL5*, and were defined as the KDM6-specific signature (Fig. 3, A to C). Conversely, other TNF/LT-induced genes were not affected, including *IL8*. Accordingly, GSK-J4 treatment led to the down-regulation of PDPN cell surface expression at D3 as measured by flow cytometry ($P < 0.001$) (Fig. 3D) but did not affect IL-8 production quantified in cell supernatants by Luminex (Fig. 3E). GSK-J4 treatment also affected the GEP of immunofibroblasts at D3 after TNF/LT treatment, with a down-regulation of a set of lymphoid stroma genes including *CXCL10*, *VCAM1*, *TNFRSF9*, *PDPN*, *IL1B*, *CCL19*, *CCL2*, and *CCL5*, unlike *IL8* (Fig. 3F, adjusted $P < 0.05$). In agreement, KDM6-specific signature was found enriched for pathways associated with NF-κB activation and TNF signaling (fig. S3, A and B). Together, these data support the hypothesis that KDM6B partially regulates immunofibroblast commitment.

KDM6B supports immunofibroblast commitment in vivo

To validate the role of KDM6B in LSC/immunofibroblast differentiation in vivo, we first used a single-cell atlas of mouse fibroblasts purified from healthy tissues and highlighted a specific enrichment of KDM6-specific signature in *Ccl19*$^+$ FRC (Fig. 4A and fig. S4A). We then used a model of TLS formation to further assess the kinetic of early immunofibroblast commitment. In this model, the infection of the salivary gland by a defective AdV5 results in the expansion and activation of a population of Pdpn$^+$ immunofibroblast progenitors, thus leading to their up-regulation of LSC markers (*12*, *38*). We sorted Cd45$^-$Cd31$^-$Epcam$^-$Pdpn$^+$ salivary gland stromal cells (*12*) (fig. S4B) before (H0) and at various time points after AdV5 injection corresponding to very early (3 hours, H3), early [day 1 (D1) and day 2 (D2)], peak [day 8 (D8)], and resolution [day 23 (D23)] of TLS ($n = 3$). Using RNA-seq, we identified 4277 genes up-regulated at any timepoint during TLS induction (adjusted $P < 0.05$, fold change >2, DESeq 2 analysis) (Fig. 4B). Among them, as observed for early response of human ASC to TNF/LT in vitro, an up-regulation of immunomodulatory chemokines and cytokines (including *Ccl2*, *Ccl5*, and *Cxcl10*), and adhesion molecules (including *Pdpn*, *Icam1*, and *Vcam1*), was detected as soon as H3 after induction (Fig. 4C and table S3). The H3 TLS signature included 2642 up-regulated genes and was enriched for TNF and NF-κB signaling pathways (fig. S4C). The human early immunofibroblast signature was found to be enriched in the GEP of Pdpn$^+$ TLS immunofibroblasts at H3, D1, and D2, unlike at D8 and D23, highlighting the similarities between murine and human early immunofibroblast commitment (fig. S4D). Next, we investigated the expression of KDM during murine immunofibroblast commitment in vivo. Notably, *Kdm6b* expression demonstrated the most substantial increase, peaking at H3 following TLS induction (Fig. 4D). Moreover, the human KDM6-specific gene signature was enriched in H3 murine Pdpn$^+$ TLS immunofibroblasts (Fig. 4E). Consistently, the KDM6-specific gene signature was enriched in FLS from patients with RA compared to osteoarthritis (OA) (*39*) ($P < 0.001$) (Fig. 4F), thereby reinforcing the hypothesis of the involvement of KDM6B in the acquisition of an inflammatory profile in RA FLS (*29*). Moreover, analysis of single-cell atlas obtained from diseased mouse and human organs (*32*) revealed a specific enrichment ($P < 0.0001$) of KDM6-specific genes in the cluster of *CCL19*$^+$ human fibroblasts, originating mostly from patients with ulcerative colitis, and in mouse *Ccl19*$^+$ fibroblasts purified in pathological contexts (Fig. 4G and fig. S4, E to G). We identified Ccl2 and Ccl5, two chemokines involved in monocyte recruitment, among the KDM6-specific genes that were the most differentially up-regulated in *Ccl19*$^+$ fibroblasts obtained from diseased organs versus healthy tissues (Fig. 4H). Furthermore, within lymph node murine LSC subsets, the KDM6-specific gene signature was found to be enriched in *Cxcl9*$^+$ T cell reticular cells, the FRC subset postulated to direct the movement of myeloid cells in inflamed lymphoid tissues ($P < 0.001$, *t* test; fig. S4H and table S4). Collectively, our findings support a role for KDM6B in the commitment of LSC/immunofibroblast precursors into myeloid-attracting cells in vivo, which could contribute to pathological chronic inflammation.

Early activation of KDM6B affects immunofibroblast immune properties

Immunofibroblasts and LSC are characterized by their capacity to interact with myeloid cells that play in turn a key role in the initiation of TLS formation (*40*). CCL2 and CCL5 induction during human immunofibroblast commitment in vitro was associated with an early recruitment of KDM6B and P300 on *CCL2* and *CCL5* enhancers, as assessed by CUT&RUN KDM6B genome-wide binding profile (fig. S2G) and confirmed by CUT&RUN quantitative polymerase chain reaction (qPCR) (Fig. 5A and fig. S5A). However, H3K27me3 was not affected at the *CCL2* and *CCL5* enhancers after TNF/LT stimulation nor under GSK-J4 treatment (fig. S5B). KDM6B was also shown to promote the demethylation of H3K27me2 into H3K27me1 (*41*). In agreement, we observed a significant decrease of H3K27me2 level on both *CCL2* enhancers and one*CCL5* enhancer upon TNF/LT treatment (Fig. 5B). These data suggest a direct involvement of KDM6B in the regulation of *CCL2* and *CCL5* expression, through H3K27me2 demethylation and H3K27 acetylation. In agreement, GSK-J4 treatment led to a specific decrease in H3K27ac at *CCL2* and *CCL5* enhancers at D3 (Fig. 5C). KDM6 inhibition by both GSK-J4 treatment and shRNA targeting KDM6B subsequently decreased CCL2 and CCL5 expression as visualized by qPCR (Fig. 5D and fig. S5, C and D) and Luminex D3 (Fig. 5E). Last, we set up a Transwell migration assay in which monocyte migration in response to ASC supernatant was dependent on CCL2, as shown by the strong reduction of monocyte recruitment in the presence of a CCR2 antagonist (Fig. 5F). GSK-J4 treatment strongly reduced the capacity of TNF/LT-stimulated ASC to promote monocyte migration ($n = 7$,

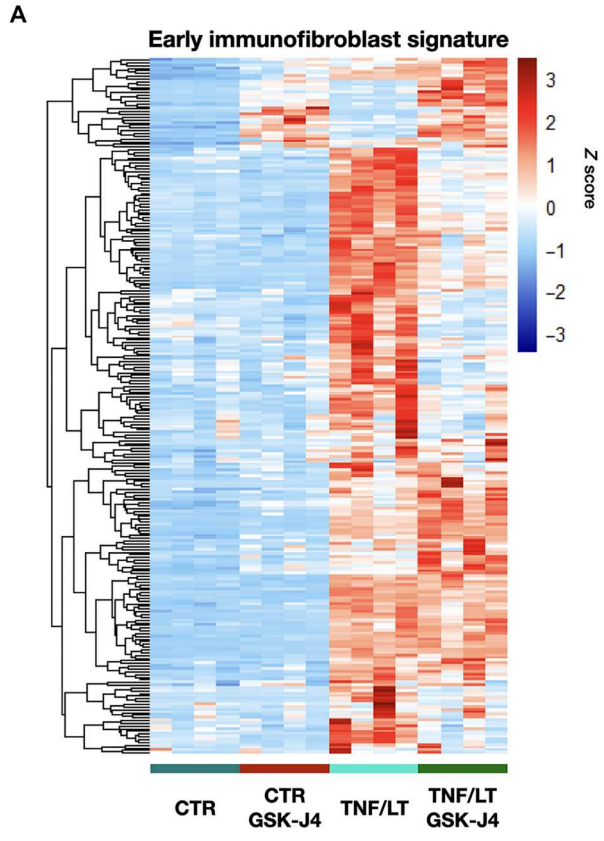

B

KDM6-specific gene signature							
ABAT	*CD82*	*EREG*	*IFIH1*	*LAMC2*	*PDPN*	*SLAMF8*	*TMEM51*
ACKR4	*CLIC6*	*FAM43A*	*IKBKE*	*LGI2*	*PRLR*	*SLC15A3*	*TNFRSF9*
APOL3	*CTSS*	*FAM65C*	*IL1B*	*LIF*	*PSMB9*	*SLC1A3*	*TNFSF4*
BCL3	*CXCL10*	*GBP4*	*IL27RA*	*LIMD2*	*PTPRE*	*SLC2A6*	*TRAF1*
BMP2	*CXCL5*	*GBP5*	*IL33*	*LRFN5*	*RAB38*	*SRGAP3*	*TRIM47*
C3	*CXCL6*	*GCH1*	*IL4I1*	*LRRN3*	*RASGRP3*	*TAPSAR1*	*TRPA1*
CCL2	*CYP1B1*	*GPR68*	*IL7*	*MOB3B*	*RCSD1*	*TGFA*	*TYMP*
CCL5	*CYP7B1*	*HERC6*	*KY*	*OAS3*	*RNF207*	*TLR3*	*VCAM1*
CCL7	*DGAT2*	*HSD11B1*	*L1TD1*	*PARP14*	*SERPINB2*	*TMEM132A*	*WTAPP1*

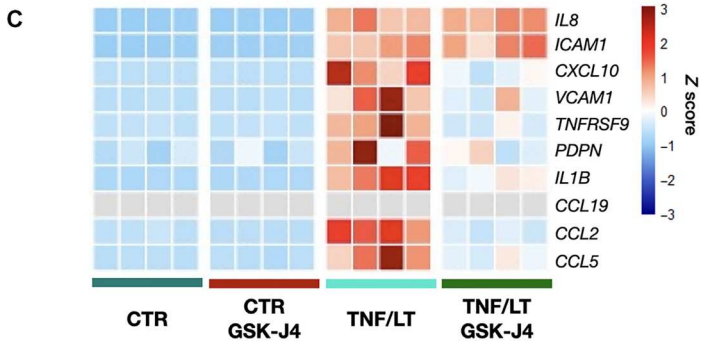

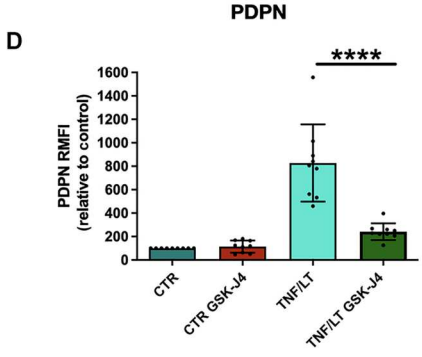

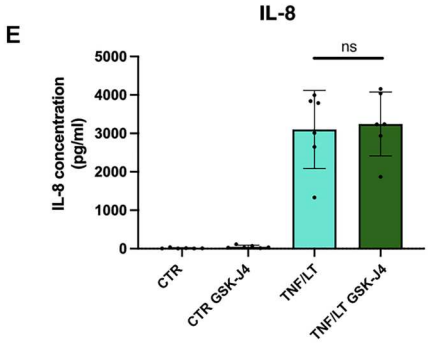

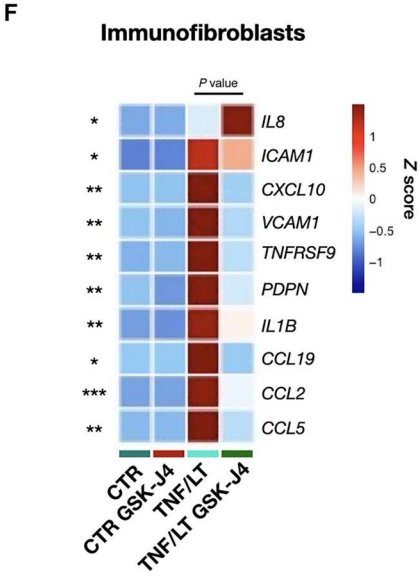

Fig. 3. KDM6B inhibition partially impairs immunofibroblast commitment in vitro. (**A**) Heatmap visualization of the expression values of genes up-regulated by 6 hours (H6) of tumor necrosis factor–α (TNF)/lymphotoxin α1β2 (LT) treatment ($n = 4$, adjusted $P < 0.05$, fold change >2, DESeq2 analysis) in the presence of the KDM6 inhibitor GSK-J4 or dimethyl sulfoxide (DMSO) as a control. *Z* score is visualized through a color code. (**B**) Table of the 72 KDM6-specific genes repressed in the presence of GSK-J4. (**C**) Heatmap of a selection of lymphoid stromal cell (LSC)/immunofibroblast gene expression as defined by RNA sequencing (RNA-seq) analysis at H6 after TNF/LT treatment in the presence of the KDM6 inhibitor GSK-J4 or DMSO as a control ($n = 4$). *Z* score is visualized through a color code. (**D**) gp38/podoplanin (PDPN) cell surface protein expression quantified by flow cytometry on adipose-derived stromal cells (ASCs) treated or not with TNF/LT for 3 days (D3), in the presence or not of the KDM6 inhibitor GSK-J4 ($n = 9$). (Values are means ± SD, ****$P < 0.0001$). (**E**) IL-8 concentration was assessed by Luminex in the supernatants of ASC treated or not with TNF/LT for D3, in the presence or not of the KDM6 inhibitor GSK-J4 ($n = 6$). Values are means ± SD, P = ns). (**F**) Expression of LSC/immunofibroblast genes in ASC treated or not with TNF/LT for D3, in the presence or not of the KDM6 inhibitor GSK-J4 ($n = 5$ for *IL1B*, *CCL5*, and *TNFRSF9*, and $n = 9$ for the others, values are mean, FDR-adjusted *$P < 0.05$, **$P < 0.01$, ***$P < 0.001$). (D to F) Statistical analyses were performed using Mann-Whitney tests.

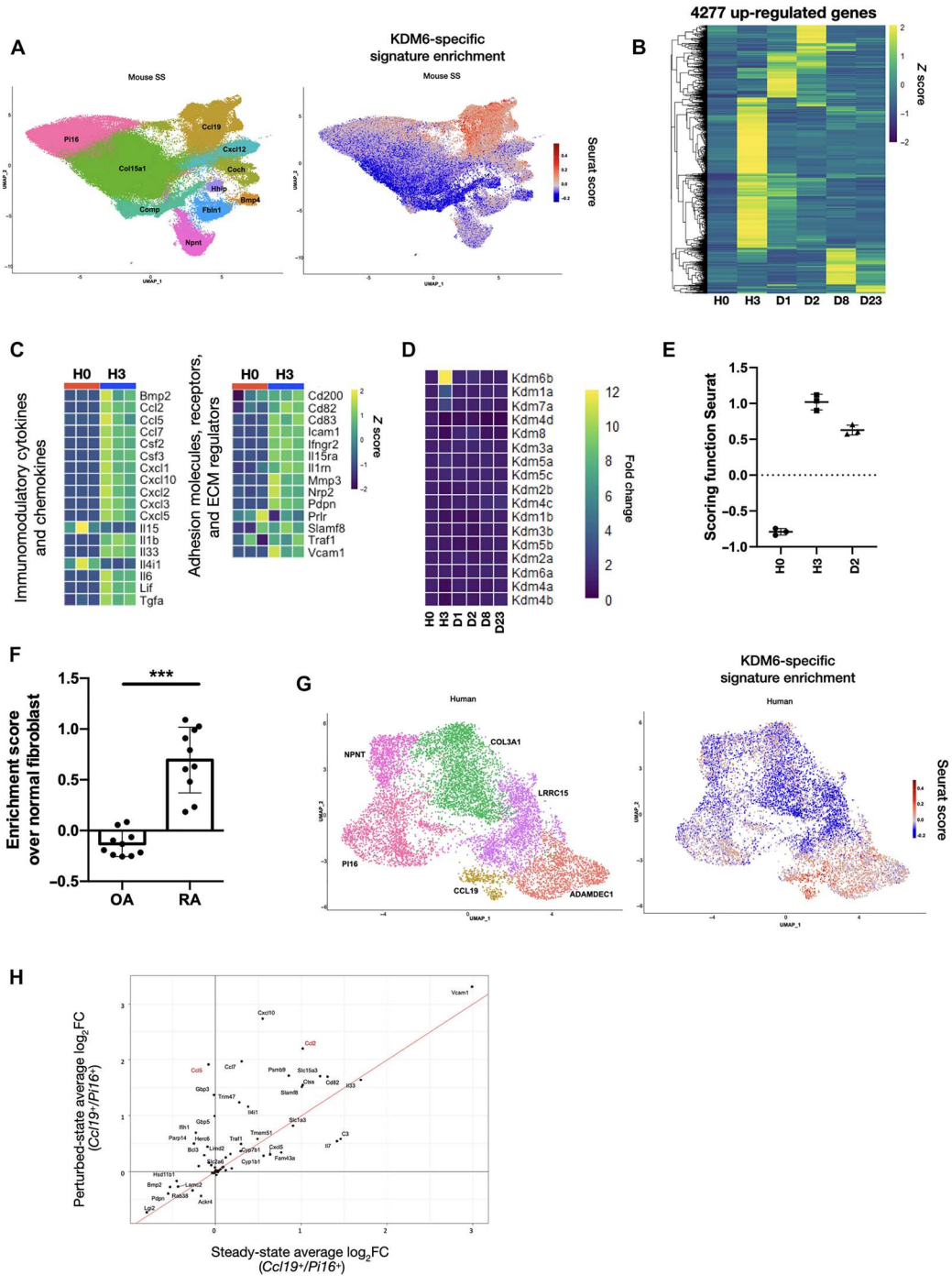

Fig. 4. KDM6B supports immunofibroblast commitment in vivo. (**A**) Seurat score enrichment of the KDM6-specific signature (right) in mouse steady-state (ss) fibroblast single-cell RNA sequencing (scRNAseq) atlas (*32*) reanalyzed by Uniform Manifold Approximation and Projection (UMAP) (left). (**B**) RNA sequencing (RNA-seq) analysis of Pdpn$^+$ fibroblasts purified from murine salivary glands at different time points before (H0) or after [3 hours (H3), 1 day (D1), 3 days (D3); 8 days (D8) and 23 days (D23)] tertiary lymphoid structure (TLS) induction (n = 3). Differentially expressed genes (adjusted P < 0.05, fold change >2 or < −2, DESeq2 analysis) were represented through an heatmap, with z score visualized through a color code. (**C**) Heatmap showing the normalized counts of selected genes in Pdpn$^+$ fibroblasts purified from murine salivary glands before (H0) and 3 hours after (H3) TLS induction (n = 3), with z score visualized through a color code. (**D**) Expression of histone lysine demethylases in Pdpn$^+$ fibroblasts purified from mouse TLS at the same time points as in (B). RNA-seq data were normalized with H0 expression as a control, and mean fold change values (n = 3) were represented according to the color code scale. (**E**) Seurat score enrichment of the KDM6-specific signature in Pdpn$^+$ fibroblasts purified from murine salivary TLS at H0, H3, and D2 (n = 3). (**F**) Seurat score enrichment of the KDM6-specific signature in fibroblast-like-synoviocytes coming from patients with osteoarthritis (OA) (n = 10) or rheumatoid arthritis (RA) (n = 10) (*39*). Normalized scores over the mean value of normal fibroblasts (n = 10) were shown (values are means ± SD, ***P < 0.001, Mann-Whitney). (**G**) Seurat score enrichment of the KDM6-specific signature (right) in scRNAseq data of human fibroblasts obtained from various diseases (*32*) reanalyzed by UMAP (left). (**H**) Dot-blot visualization of the KDM6-specifique signature in scRNA-seq atlas of mouse fibroblasts in perturbed states versus steady-state (*32*). Each gene was represented as $\log_2$ fold change enrichment of the mean expression in the *Ccl19*$^+$ cluster toward the *Pi16*$^+$ cluster.

P < 0.01). Together, these data confirm a role for KDM6B-dependent epigenetic regulation in the commitment of immunofibroblast precursors into myeloid-attracting cells.

DISCUSSION

Our study explores how epigenetic mechanisms, in particular KDM6B-dependent regulation of H3K27 histone mark, contribute to the commitment of human and murine stromal precursors into immune-competent LSC/immunofibroblasts in both normal and inflammatory contexts. The LT pathway regulates early-life programming of mesenteric lymph node stromal cells and imprints their adult transcriptomic profile and the resulting mucosal immunity (*42*). In addition, the remodeling of the mature LSC network is influenced by previous exposure to infection (*43*). This inflammatory training of LSC has recently been linked to increased levels of

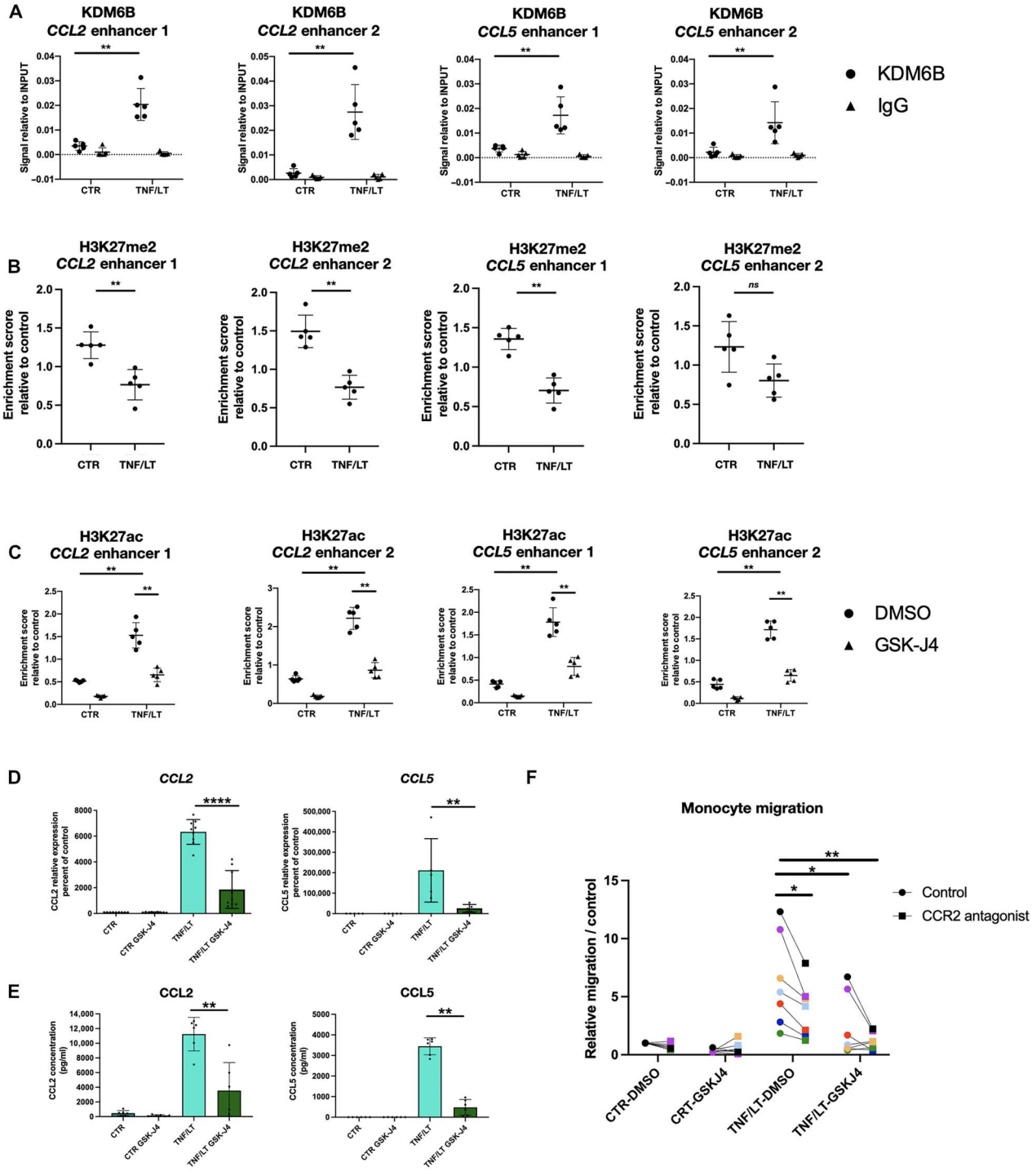

Fig. 5. Early activation of KDM6B affects immunofibroblast immune properties. (**A**) KDM6B enrichment on *CCL2* and *CCL5* regulatory elements obtained by CUT&RUN quantitative polymerase chain reaction (qPCR) in adipose-derived stromal cells (ASCs) treated or not (CTR) with tumor necrosis factor–α (TNF)/lymphotoxin α1β2 (LT) for 6 hours (H6) ($n = 5$). Immunoglobulin G (IgG) was used as negative control. (**B**) H3K27me2 enrichment on *CCL2* and *CCL5* regulatory elements obtained by CUT&RUN qPCR in ASCs treated or not with TNF/LT for 3 days (D3) ($n = 5$). Enrichment was normalized to a positive control region (*MYT1*). (**C**) H3K27ac enrichment on *CCL2* and *CCL5* regulatory elements obtained by CUT&RUN qPCR in ASCs treated or not (CTR) with TNF/LT for D3, in the presence or not of the KDM6 inhibitor GSK-J4 ($n = 5$). Enrichment was normalized to a positive control region (*ACTB*). (**D**) RT-qPCR of *CCL2* ($n = 9$) and *CCL5* ($n = 5$ in ASC treated or not (CTR) with TNF/LT for D3 in the presence or not of the KDM6 inhibitor GSK-J4. (**E**) CCL2 and CCL5 concentration were assessed by Luminex in supernatants of ASC treated or not (CTR) with TNF/LT for D3, in the presence or not of the KDM6 inhibitor GSK-J4 ($n = 6$). (**F**) Migration of monocytes purified from healthy donor peripheral blood in response to supernatants collected from ASCs treated or not (CTR) with TNF/LT for D3, in the presence or not of the KDM6 inhibitor GSK-J4. When indicated, a specific CCR2 antagonist was added. Cell migration index is calculated as the number of $DAPI^{-}CD14^{+}$ viable monocytes migrating in response to cell supernatants divided by their number in response to migration medium ($n = 7$). (A) to (F) Statistical analyses were performed using Mann-Whitney tests or Wilcoxon matched-pairs signed rank tests (values are means ± SD, $^{*}P < 0.05$, $^{**}P < 0.01$, $^{****}P < 0.0001$).

H3K4me3 and metabolic response to secondary infections (*36*). However, the underlying molecular mechanisms and the initial stage of LSC differentiation affected by these modifications have not been explored. To what extent KDM6B is the sole driver of such stroma-dependent innate immune training in the context of normal immune response remains to be studied. In this regard, we described here the TNF/LT-dependent earliest stages of immunofibroblast commitment in vitro and in vivo. However, additional external stimuli, produced by infiltrating immune cells, and other molecular/epigenetic drivers would be required to trigger the terminal differentiation and maintain the functional phenotype of immune stroma. Apart from the molecular profiling of normal human and murine immunofibroblast commitment, we identified the KDM6B-specific gene signature as enriched in pathological contexts, including in RA fibroblasts, and in *CCL19*$^+$ disease-related fibroblasts identified in autoimmune colitis (*32*). *CCL19*$^+$ fibroblasts are also commonly found in Sjögren′s syndrome, a disease mimicked by the in vivo salivary TLS model (*44*). The involvement of KDM6B or other epigenetic modulators in the initiation, maintenance, or reactivation of pathogenic LSC-like stroma during chronic inflammation is not yet clear. To this end, the use of KDM6B deletion in Fap$^+$ or Ccl19$^+$ precursor cells (*45*, *46*) would be useful to decipher the cell fate of acutely or chronically activated LSC/immunofibroblast precursors in the absence of KDM6B.

Here, we proposed that KDM6B directly bound to regulatory elements, particularly gene enhancers, related to the immunofibroblast phenotype, and that GSK-J4 treatment could prevent immunofibroblast commitment by abrogating immunofibroblast gene enhancer acetylation. Nevertheless, how KDM6B is specifically addressed to chromatin in response to TNF/LT treatment need to be fully elucidated. TNF and LT synergistically activate canonical and noncanonical NF-κB pathways, both required for LSC differentiation (*47*). Analysis of the motifs of KDM6B binding sites highlighted a strong association with NF-κB motifs, suggesting that KDM6B could be targeted to LSC/immunofibroblast genes through NF-κB members. It has been previously shown that KDM6B interacts with RELA to induce the transcription of inflammatory genes in response to TNF in keratinocytes through histone demethylation activity (*26*). Although KDM6B was initially described as an H3K27me3 demethylase, we observed no modification in the levels of H3K27me3 during immunofibroblast commitment at CCL2 and CCL5 enhancers. However, KDM6B also regulates the level of H3K27me2 in infected epithelial cells (*41*), and we noticed that H3K27me2 levels decreased upon TNF/LT stimulation, concomitant with a gain of H3K27 acetylation. Together, our data support the importance of KDM6B for CCL2 and CCL5 regulation. However, the molecular interplay between KDM6B, NF-κB members, and C/EBPβ/P300, for the regulation of H3K27 modifications necessitates further investigation.

Last, we observed that KDM6B was involved in the epigenetic control of CCL2 in differentiating immunofibroblasts, leading to early monocyte recruitment. Spleen red pulp fibroblasts participate in the maintenance of red pulp macrophage network through expression of CCL2 and CCL7 (*48*). Furthermore, CCL2-mediated recruitment of monocytes by LSC (*49*) is involved in the prevention of an excessive immune response, a mechanism that could be dysregulated in autoimmune diseases. In intestinal injury, MSCs support the polarization of IL-10–releasing macrophages through the production of heterodimers of CCL2 and CXCL12 (*50*). FLS-derived CXCL12 is also involved in the recruitment of monocytes in the synovium of RA (*51*). KDM6B is thought to regulate CXCL12 in glioblastoma cells (*52*), suggesting that it could affect both CCL2 and CXCL12 production. These findings, together with the identification of an enrichment of KDM6B-specific gene signature in RA FLS, suggest that KDM6B could be a relevant target in autoimmune diseases, as recently proposed in a model of inflammation-induced mastitis (*53*). In addition, the overexpression of CCL2 in mesenchymal precursors has been associated with the phenotype of cancer-associated fibroblasts. Tumor-infiltrating stromal cells overexpress CCL2 in a mouse lymphoma model, leading to macrophage recruitment through the CCR2 axis (*54*). Similarly, follicular lymphoma B cells trigger CCL2 expression in human stromal cells and induce monocyte recruitment, altogether organizing follicular lymphoma cell niches in invaded lymph nodes and bone marrow (*55*). More recently, in multiple myeloma, a subset of inflamed bone marrow stromal cells activated by TNF and IL-1β has been shown to express CCL2 and to interact with myeloid cells (*56*). Whether KDM6B is involved in this process has not been explored yet. Inhibition of KDM6B is already a promising therapeutic option in B cell lymphoma due to its direct effect on tumor B cells. KDM6B promotes survival of malignant B cells from aggressive diffuse large B cell lymphoma (*57*), and its inhibition sensitizes diffuse large B cell lymphoma to chemotherapeutic agents (*58*). Understanding the epigenetic and molecular mechanisms driving immunofibroblast LSC/immunofibroblast commitment and immune properties would be a prerequisite to boost vaccine responses or to reprogram these cells in pathological settings.

MATERIALS AND METHODS

Human tissue and cell samples

Patients were recruited under institutional review board approval following the informed consent process according to the Declaration of Helsinki and the French National Cancer Institute ethics committee recommendations. Lipoaspirations were performed in adults undergoing abdominal dermolipectomy. ASCs were obtained from the stromal vascular fraction of adipose tissue obtained from lean donors essentially as described (*18*, *59*) and were amplified in a modified Minimum Essential Medium Eagle (Gibco) supplemented with 10% fetal calf serum (FCS) (Biosera) and basic fibroblast growth factor (bFGF) (1 ng/ml; Cellgenix). ASCs were then used between passages 1 and 3 for all experiments that were run in the same medium without supplementation in bFGF. Peripheral blood monocytes from healthy donors were purified by using monocyte isolation kit II (Miltenyi Biotech) and were used directly for migration assay.

Stromal cell culture

ASCs were treated by TNF (5 ng/ml)/lymphotoxin α1β2 (LT) (50 ng/ml) (R&D Systems) and collected at different time points. When indicated, the KDM6 inhibitor GSK-J4 (20 μM) (Tocris) or dimethyl sulfoxide as a control were added each day. ASCs were also treated by a panel of other pro/anti-inflammatory factors including IFN-γ (100 IU/ml), LPS (10 ng/ml), Poly I:C (1 μg/ml), and IL-17 (10 ng/ml, R&D Systems).

Mice and TLS induction

C57BL/6 mice were bred and maintained under specific pathogen–free conditions in the Biomedical Service Unit at the University of Birmingham according to Home Office and local ethics committee regulations. The submandibular glands of mice (8 to 12 weeks old) were intraductally cannulated with 10^8 to 10^9 plaque-forming units of replication-defective adenovirus (AdV5), as previously described (*38*), to induce the formation of ectopic TLS. Tissue digestion was performed in RPMI 1640 medium containing dispase (0.8 mg/ml), collagenase P (0.2 mg/ml), and deoxyribonuclease I (DNase I) (0.1 mg/ml) and 2% (v/v) FCS for 20 min at 37°C with gentle stirring. After 20 min, the tissue fragments were pipetted very gently to further disrupt the tissue and release most cells. The tubes were placed in the water bath to allow large fragments to settle for 30 s, then the supernatant was removed and put in a 50-ml falcon tube that was filled with 10 ml of ice-cold wash buffer [0.5% (w/v) bovine serum albumin and 2 mM EDTA in phosphate-buffered saline] and had a 7-μm strainer. Fresh enzyme mix [2 ml; RPMI 1640 medium containing dispase (0.8 mg/ml), collagenase P (0.2 mg/ml), and DNase I (0.1 mg/ml)] and 2% (v/v) FCS was added to the digestion tubes, and the contents were gently mixed and incubated for 10 min. Tissue was vigorously pipetted in digestion media using a 1-ml pipette to completely digest tissue fragments. Cell suspension was transferred to the 50-ml Falcon tube from previous step. Each 50-ml tube now contained the entire cellular contents of the digested tissue. Collection tubes were centrifuged at 1800 rpm for 10 min at 4°C. Cells were stained with viability dye eFluor 780 (eBiosciences) as per manufacturer′s instructions followed by antibody staining for CD45 (30-F11, RRID:AB_893344), CD326/Epcam (G8.8, RRID:AB_1134102), CD31 (390, RRID:AB_2910329), and Pdpn (gp38; 8.1.1, RRID:AB_2161928) all from BioLegend. Stained cells were sorted using BD FACSAria. The purity of $Pdpn^+Cd31^-Epcam^-Cd45^-$ sorted stromal cells routinely exceeded 96%.

Real-time qPCR

RNA was extracted from human ASC by using NucleoSpin RNA Plus Kit (Macherey-Nagel). cDNA was synthesized by using Superscript II reverse transcriptase and Oligo-dT primers (Life Technologies). q-PCR was then performed using SYBR Green Master Mix (Life Technologies) and gene-specific primers (Eurogentec) listed in table S5. Gene expression was measured by using a StepOnePlus (Life Technologies). For each sample, expression of the genes of interest was determined from a standard curve of a pool of RNA samples and normalized to the mean value of the housekeeping gene *RPLP0*.

When indicated, gene expression was assessed by using the Fluidigm BioMark HD system. In this case, cDNAs were obtained by using the Fluidigm reverse transcription Master Mix and were then preamplified for 12 cycles in the presence of Pre-Amp Master Mix and pooled primers mix. Gene expression was then measured with the EvaGreen Master Mix on a 96.96 Dynamic Array IFC. After quality control check, gene expression was calculated with the ΔCt calculation method with *RPLP0* as the housekeeping gene.

Flow cytometry

Viable cells were analyzed after $DAPI^+$ cell exclusion (Life Technologies) by using the following monoclonal antibodies: phycoerythrin-conjugated anti-PDPN (clone NZ-1.3, RRID:AB_1582262, Ebiosciences) for ASC and immunofibroblast staining and phycoerythrin-conjugated anti-CD14 (clone M5E2, RRID:AB_396848, BD Pharmingen) for monocyte staining. Appropriate isotype-matched monoclonal antibodies were used to obtain mean fluorescence intensity ratios, and cell counts were performed with flow count fluorospheres (Beckman Coulter) to determine an index of monocyte migration. Analyses were performed by using CytoFLEX or Gallios (Beckman Coulter) flow cytometers.

RNA sequencing

Two experiments of stromal cell stimulation were performed. First, three independent ASC batches were treated or not with TNF/LT treatment for D3. Then, four independent ASC batches were treated or not with TNF/LT in the presence or not of the KDM6 inhibitor GSK-J4 for H6 RNA extraction was performed with the NucleoSpin RNA Plus kit (Macherey-Nagel), and the purity and integrity of RNA were checked with the Bioanalyzer 2100 (Agilent Technologies). All libraries and sequencing were performed by Institut Curie (Paris, France). Briefly, RNA-seq libraries were sequenced with 2 × 100-bp paired reads on the Illumina Hiseq 2500 sequencer generating more of 45 million reads per sample with >80% of sequences achieving > Q30 Phred quality scores. Raw sequencing read data were checked and visualized for quality using FastQC (v0.11.5). The bulk RNA next-generation sequencing reads were aligned to the reference genome GRCh37 release 87 using STAR (v2.5.2). Read summarization, gene and transcript counts were performed using the featureCounts (version 1.5.0). Differential gene expression was analyzed using the DESeq2 algorithm (v1.22.2). Significant genes were defined as $P < 0.01$ after adjustment for false discovery by Bonferroni correction. For sorted native ASC, these cells were aligned with human LSC subsets from GSE148656 (*33*) to the reference genome GRCh38 release 90 using STAR (v2.5.2).

For the mouse study, after sorting of the $Pdpn^+$ stromal cells at different time points post TLS induction, RNA extraction was performed with the NucleoSpin RNA Plus mini kit (Macherey-Nagel), and the purity and integrity of RNA were checked with the Bioanalyzer 2100 (Agilent Technologies). Raw sequencing read data were checked and visualized for quality using FastQC (v0.11.5). The bulk RNA next-generation sequencing reads were aligned to the reference genome GRCm38 release 100 using STAR (v2.5.2). Read summarization as well as gene and transcripts counts were performed using the featureCounts (version 1.5.0). Differential gene expression was analyzed using the DESeq2 algorithm (v1.22.2). Significant genes were defined as $P < 0.05$ after adjustment for false discovery by Benjamini-Hochberg correction.

CUT&RUN

CUT&RUN protocol (*37*) was used with minor modifications. Briefly, ASC were committed into (early or late) immunofibroblasts, and when specify KDM6 inhibitor GSK-J4 was added. Briefly, cells (1.10^3) were bound to Concanavalin A beads (Polysciences) and incubated with 2 μl of anti-H3K27ac (Cell Signaling Technology, D5E4, RRID:AB_10949503), 2-μl anti-H3K27me3 (Cell Signaling Technology, C36B1, RRID:AB_2616029), or 2-μl anti-H3K27me2 (Diagenode, C15410046, polyclonal) antibodies for 1 hour at room temperature, or with 1 μl of anti-KDM6B (Abcam, ab38113, RRID:AB_943898) or 2 μl of p300 (Diagenode, C15200211) antibodies, overnight at 4°C. For each experiment, a

negative immunoglobulin G (IgG) control Rabbit antibody was used (DA1E, Cell Signaling Technology, RRID:AB_1550038). pA/G-MNase (0.89 ng/μl) was bound to antibodies and activated with $CaCl_2$ to digest chromatin during 30 min at 0°C. Enzymatic reaction was stopped, and chromatin fragments were released by an incubation of 10 min at 37°C. Chromatin sonication was performed with the EpiShear Probe Sonicator (Active Motif). DNA was purified with MinElute PCR Purification Kit (Qiagen). All primers used in this study are listed in table S6. For KDM6B *CUT&RUN* experiments, eluted DNA fragments were subjected to NGS sequencing, libraries were prepared by INTEGRAGEN, using the NEBNext Ultra II DNA Library Prep Kit, containing end preparation, A tailing and Illumina indexed adapters ligation step. After concentration measurement by qPCR, libraries are sequenced on an illumina NovaSeq as paired-end 100pb reads.

CUT&RUN-seq data analysis

FASTQC (v 0.11.5) was used to check reads quality, and reads with low quality were discarded. CUT&RUN-seq reads were then aligned to the human genome (hg19) using the Bowtie2 tool, and peak were identified with MACS2, using input as background, only peaks with a minimum FDR < 10^{-5} were keep. The R package ChIPseeker (*60*) (v4.1) with the function annotatePeak() was then used to annotate peak with their genomic locations and to associate them to the closer gene. Differential peak binding was then performed with DESeq2 algorithm (v1.22.2). Significant peaks were defined as $P <$ 0.05 after adjustment for false discovery by Benjamini-Hochberg correction. DeepTools 3.5.0 (*61*) was then used with the function computeMatrix to calculate KDM6B enrichment around specific region of the genome (−2 kb/+2Kb), scores were then visualized with the function plotHeatmap and plotProfiles. KDM6B binding profile as bigwig file was also visualized at specific gene by using integrative Genomics Viewer (https://igv.org/app/). Primers were designed in these regions and used for CUT&RUN-qPCR experiments.

Microarray analysis

Raw microarray data corresponding to of ASC and adipocyte (GSE 77532) as well as healthy fibroblasts, OA, and RA FLS (GSE 55235) were downloaded from the National Center for Biotechnology Information Gene Expression Omnibus (GEO) database. Arrays were normalized according to the GC-RMA normalization procedure Subsequent normalized matrix was then used for Seurat enrichment analysis. For each gene, the probeset with the highest expression was retained. Normalized data were then used for subsequent enrichment analysis. For GSE 77523, differential analysis of gene expression levels was then carried out with the Limma package in R software. *P* values adjusted by Benjamini and Hochberg < 0.05 were considered statistically significant.

Data visualization and representation

Visualization of differentially expressed genes was done using the pheatmap and ggplot R package. Venn diagrams were obtained with InteractiVenn (www.interactivenn.net/). Enrichment of the KDM6-specific gene signature was computed with the Seurat R package (V4.0). Briefly, bulk transcriptomic data were converted into a Seurat object and Signature scores were computed with the AddModuleScore function of the Seurat R package. This function calculates for each individual sample the average expression of each gene signature, subtracted by the aggregated expression of control gene sets. All the analyzed genes were binned into 25 bins based on their averaged expression, and for each gene of the gene signature, 100 control genes were randomly selected from the same bin as the gene. When necessary, gene names were converted to their mouse equivalent with a home-made R script and the homologene package. Sample scores were then visualized through GraphPad.

Transcription factor enrichment

Enrichment for TF motifs was evaluated with HOMER (*61*) by using the command findMotifs.pl with default parameter and the addition of the -bg parameter for background correction with the list of al identify peak. Enrichment for TF targets from transcriptomic data was performed with Enrichr (https://maayanlab.cloud/Enrichr/) by interrogating the TRRUST (*62*) Transfection Factor 2019 database.

Chemokine quantification

IL-8, CCL2, and CCL5 were quantified by multiplex enzyme-linked immunosorbent assay (Luminex, Millipore) in the supernatants of ASC stimulated or not with TNF/LT in the presence or not of the KDM6 inhibitor GSK-J4 during D3.

Migration assay

Freshly purified peripheral blood monocytes (10^5 cells/100 μl) were added in RPMI–1% FCS (monocyte migration medium) to the upper compartment of Transwell chambers with 5-μm pore filters. Lower chambers contained supernatants from stromal cells primed for D3 by TNF/LT with or without KDM6 inhibition by GSK-J4 in RPMI-1% FCS. CCR2 receptor on monocytes was blocked or not by a pretreatment (10 min) with a specific CCR2 antagonist (Sigma-Aldrich, sc-202525) at 10 nM. The absolute number of $DAPI^-$ $CD14^+$ viable monocytes in the lower Transwell chamber was quantified by flow cytometry using FlowCount beads after 2 hours of migration. Cell migration index was calculated as the number of $DAPI^-CD14^+$ viable cells migrating in response to cell supernatants divided by their number in response to migration medium.

Statistical analysis

Statistical analyses were performed with GraphPad Prism 6.0 software using the nonparametric Wilcoxon test for matched pairs or the Mann-Whitney nonparametric *U* test as appropriate.

Supplementary Materials

This PDF file includes:

Supplementary Materials and Methods
Figs. S1 to S5
Legends for tables S1 to S3
Tables S4 to S6

Other Supplementary Material for this manuscript includes the following:

Tables S1 to S3

REFERENCES AND NOTES

1. R. Roozendaal, R. E. Mebius, Stromal cell-immune cell interactions. *Annu. Rev. Immunol.* **29**, 23–43 (2011).
2. L. B. Rodda, E. Lu, M. L. Bennett, C. L. Sokol, X. Wang, S. A. Luther, B. A. Barres, A. D. Luster, C. J. Ye, J. G. Cyster, Single-cell RNA sequencing of lymph node stromal cells reveals niche-associated heterogeneity. *Immunity* **48**, 1014–1028.e6 (2018).
3. H.-Y. Huang, A. Rivas-Caicedo, F. Renevey, H. Cannelle, E. Peranzoni, L. Scarpellino, D. L. Hardie, A. Pommier, K. Schaeuble, S. Favre, T. K. Vogt, F. Arenzana-Seisdedos, P. Schneider, C. D. Buckley, E. Donnadieu, S. A. Luther, Identification of a new subset of lymph node stromal cells involved in regulating plasma cell homeostasis. *Proc. Natl. Acad. Sci. U.S.A.* **115**, E6826–E6835 (2018).
4. L. B. Rodda, O. Bannard, B. Ludewig, T. Nagasawa, J. G. Cyster, Phenotypic and morphological properties of germinal center dark zone Cxcl12-expressing reticular cells. *J. Immunol.* **195**, 4781–4791 (2015).
5. N. B. Pikor, H.-W. Cheng, L. Onder, B. Ludewig, Development and immunological function of lymph node stromal cells. *J. Immunol.* **206**, 257–263 (2021).
6. N. B. Pikor, U. Mörbe, M. Lütge, C. Gil-Cruz, C. Perez-Shibayama, M. Novkovic, H.-W. Cheng, C. Nombela-Arrieta, T. Nagasawa, M. A. Linterman, L. Onder, B. Ludewig, Remodeling of light and dark zone follicular dendritic cells governs germinal center responses. *Nat. Immunol.* **21**, 649–659 (2020).
7. Y. Abe, M. Sakata-Yanagimoto, M. Fujisawa, H. Miyoshi, Y. Suehara, K. Hattori, M. Kusakabe, T. Sakamoto, H. Nishikii, T. B. Nguyen, Y. Owada, T. Enomoto, A. Sawa, H. Bando, C. Yoshida, R. Tabata, T. Terao, M. Nakayama, K. Ohshima, K. Usuki, T. Oda, K. Matsue, S. Chiba, A single-cell atlas of non-haematopoietic cells in human lymph nodes and lymphoma reveals a landscape of stromal remodelling. *Nat. Cell Biol.* **24**, 565–578 (2022).
8. C. Bénézech, A. White, E. Mader, K. Serre, S. Parnell, K. Pfeffer, C. F. Ware, G. Anderson, J. H. Caamaño, Ontogeny of stromal organizer cells during lymph node development. *J. Immunol.* **184**, 4521–4530 (2010).
9. C. Bénézech, E. Mader, G. Desanti, M. Khan, K. Nakamura, A. White, C. F. Ware, G. Anderson, J. H. Caamaño, Lymphotoxin-β receptor signaling through NF-κB2-RelB pathway reprograms adipocyte precursors as lymph node stromal cells. *Immunity* **37**, 721–734 (2012).
10. C. Bénézech, N.-T. Luu, J. A. Walker, A. A. Kruglov, Y. Loo, K. Nakamura, Y. Zhang, S. Nayar, L. H. Jones, A. Flores-Langarica, A. McIntosh, J. Marshall, F. Barone, G. Besra, K. Miles, J. E. Allen, M. Gray, G. Kollias, A. F. Cunningham, D. R. Withers, K. M. Toellner, N. D. Jones, M. Veldhoen, S. A. Nedospasov, A. N. J. McKenzie, J. H. Caamaño, Inflammation-induced formation of fat-associated lymphoid clusters. *Nat. Immunol.* **16**, 819–828 (2015).
11. C. Gago da Graça, L. G. M. van Baarsen, R. E. Mebius, Tertiary lymphoid structures: Diversity in their development, composition, and role. *J. Immunol.* **206**, 273–281 (2021).
12. S. Nayar, J. Campos, C. G. Smith, V. Iannizzotto, D. H. Gardner, F. Mourcin, D. Roulois, J. Turner, M. Sylvestre, S. Asam, B. Glaysher, S. J. Bowman, D. T. Fearon, A. Filer, K. Tarte, S. A. Luther, B. A. Fisher, C. D. Buckley, M. C. Coles, F. Barone, Immunofibroblasts are pivotal drivers of tertiary lymphoid structure formation and local pathology. *Proc. Natl. Acad. Sci. U. S.A.* **116**, 13490–13497 (2019).
13. S. Davidson, M. Coles, T. Thomas, G. Kollias, B. Ludewig, S. Turley, M. Brenner, C. D. Buckley, Fibroblasts as immune regulators in infection, inflammation and cancer. *Nat. Rev. Immunol.* **21**, 704–717 (2021).
14. J. C. Martin, C. Chang, G. Boschetti, R. Ungaro, M. Giri, J. A. Grout, K. Gettler, L.-S. Chuang, S. Nayar, A. J. Greenstein, M. Dubinsky, L. Walker, A. Leader, J. S. Fine, C. E. Whitehurst, M. L. Mbow, S. Kugathasan, L. A. Denson, J. S. Hyams, J. R. Friedman, P. T. Desai, H. M. Ko, I. Laface, G. Akturk, E. E. Schadt, H. Salmon, S. Gnjatic, A. H. Rahman, M. Merad, J. H. Cho, E. Kenigsberg, Single-cell analysis of Crohn's disease lesions identifies a pathogenic cellular module associated with resistance to anti-TNF therapy. *Cell* **178**, 1493–1508.e20 (2019).
15. L. Peduto, S. Dulauroy, M. Lochner, G. F. Späth, M. A. Morales, A. Cumano, G. Eberl, Inflammation recapitulates the ontogeny of lymphoid stromal cells. *J. Immunol.* **182**, 5789–5799 (2009).
16. A. B. Rodriguez, J. D. Peske, A. N. Woods, K. M. Leick, I. S. Mauldin, M. O. Meneveau, S. J. Young, R. S. Lindsay, M. M. Melssen, S. Cyranowski, G. Parriott, M. R. Conaway, Y.-X. Fu, C. L. Slingluff, V. H. Engelhard, Immune mechanisms orchestrate tertiary lymphoid structures in tumors via cancer-associated fibroblasts. *Cell Rep.* **36**, 109422 (2021).
17. C. Ménard, J. Dulong, D. Roulois, B. Hébraud, L. Verdière, C. Pangault, V. Sibut, I. Bezier, N. Bescher, C. Monvoisin, M. Gadelorge, N. Bertheuil, E. Flécher, L. Casteilla, P. Collas, L. Sensebé, P. Bourin, N. Espagnolle, K. Tarte, Integrated transcriptomic, phenotypic, and functional study reveals tissue-specific immune properties of mesenchymal stromal cells. *Stem Cells* **38**, 146–159 (2020).
18. S. Pandey, F. Mourcin, T. Marchand, S. Nayar, M. Guirriec, C. Pangault, C. Monvoisin, P. Amé-Thomas, F. Guilloton, J. Dulong, M. Coles, T. Fest, A. Mottok, F. Barone, K. Tarte, IL-4/CXCL12 loop is a key regulator of lymphoid stroma function in follicular lymphoma. *Blood* **129**, 2507–2518 (2017).
19. H. Wang, Y. Yang, J. Liu, L. Qian, Direct cell reprogramming: Approaches, mechanisms and progress. *Nat. Rev. Mol. Cell Biol.* **22**, 410–424 (2021).
20. Z. H. Zheng, T. W. Sam, Y. Zeng, J. J. H. Chu, Y.-H. Loh, Chromatin regulation in development: Current understanding and approaches. *Stem Cells Int.* **2021**, 8817581 (2021).
21. D. Yang, H. Okamura, Y. Nakashima, T. Haneji, Histone demethylase Jmjd3 regulates osteoblast differentiation via transcription factors *Runx2* and osterix. *J. Biol. Chem.* **288**, 33530–33541 (2013).
22. F. Zhang, L. Xu, L. Xu, Q. Xu, D. Li, Y. Yang, G. Karsenty, C. D. Chen, JMJD3 promotes chondrocyte proliferation and hypertrophy during endochondral bone formation in mice. *J. Mol. Cell Biol.* **7**, 23–34 (2015).
23. L. Ye, Z. Fan, B. Yu, J. Chang, K. Al Hezaimi, X. Zhou, N.-H. Park, C.-Y. Wang, Histone demethylases KDM4B and KDM6B promotes osteogenic differentiation of human MSCs. *Cell Stem Cell* **11**, 50–61 (2012).
24. Z. Liu, H.-L. Lee, J. S. Suh, P. Deng, C.-R. Lee, O. Bezouglaia, M. Mirnia, V. Chen, M. Zhou, Z.-K. Cui, R. H. Kim, M. Lee, T. Aghaloo, C. Hong, C.-Y. Wang, The ERα/KDM6B regulatory axis modulates osteogenic differentiation in human mesenchymal stem cells. *Bone Res.* **10**, 3 (2022).
25. F. De Santa, M. G. Totaro, E. Prosperini, S. Notarbartolo, G. Testa, G. Natoli, The histone H3 lysine-27 demethylase Jmjd3 links inflammation to inhibition of polycomb-mediated gene silencing. *Cell* **130**, 1083–1094 (2007).
26. J. Na, J. Y. Shin, H. Jeong, J. Y. Lee, B. J. Kim, W. S. Kim, T. Y. Yune, B.-G. Ju, JMJD3 and NF-κB-dependent activation of Notch1 gene is required for keratinocyte migration during skin wound healing. *Sci. Rep.* **7**, 6494 (2017).
27. C.-A. Malinczak, A. J. Rasky, W. Fonseca, M. A. Schaller, R. M. Allen, C. Ptaschinski, S. Morris, N. W. Lukacs, Upregulation of H3K27 demethylase KDM6 during respiratory syncytial virus infection enhances proinflammatory responses and immunopathology. *J. Immunol.* **204**, 159–168 (2020).
28. C. Bergmann, A. Brandt, B. Merlevede, L. Hallenberger, C. Dees, T. Wohlfahrt, S. Pötter, Y. Zhang, C.-W. Chen, T. Mallano, R. Liang, R. Kagwiria, A. Kreuter, I. Pantelaki, A. Bozec, D. Abraham, R. Rieker, A. Ramming, O. Distler, G. Schett, J. H. W. Distler, The histone demethylase Jumonji domain-containing protein 3 (JMJD3) regulates fibroblast activation in systemic sclerosis. *Ann. Rheum. Dis.* **77**, 150–158 (2018).
29. W. Jia, W. Wu, D. Yang, C. Xiao, Z. Su, Z. Huang, Z. Li, M. Qin, M. Huang, S. Liu, F. Long, J. Mao, X. Liu, Y. Z. Zhu, Histone demethylase JMJD3 regulates fibroblast-like synoviocyte-mediated proliferation and joint destruction in rheumatoid arthritis. *FASEB J.* **32**, 4031–4042 (2018).
30. C. Loh, S.-H. Park, A. Lee, R. Yuan, L. B. Ivashkiv, G. D. Kalliolias, TNF-induced inflammatory genes escape repression in fibroblast-like synoviocytes: Transcriptomic and epigenomic analysis. *Ann. Rheum. Dis.* **78**, 1205–1214 (2019).
31. R. Foxall, P. Narang, B. Glaysher, E. Hub, E. Teal, M. C. Coles, M. Ashton-Key, S. A. Beers, M. S. Cragg, Developing a 3D B cell lymphoma culture system to model antibody therapy. *Front. Immunol.* **11**, 605231 (2020).
32. M. B. Buechler, R. N. Pradhan, A. T. Krishnamurty, C. Cox, A. K. Calviello, A. W. Wang, Y. A. Yang, L. Tam, R. Caothien, M. Roose-Girma, Z. Modrusan, J. R. Arron, R. Bourgon, S. Müller, S. J. Turley, Cross-tissue organization of the fibroblast lineage. *Nature* **593**, 575–579 (2021).
33. F. Mourcin, L. Verdière, D. Roulois, R. Amin, C. Lamaison, V. Sibut, B. Thamphya, C. Pangault, C. Monvoisin, S. Huet, M. Seffals, S. Baulande, F. Mechta-Grigoriou, P. Legoix, D. Rossille, M. Guirriec, S. Léonard, G. Cartron, G. Salles, T. Fest, K. Tarte, Follicular lymphoma triggers phenotypic and functional remodeling of the human lymphoid stromal cell landscape. *Immunity* **54**, 1788–1806.e7 (2021).
34. M. A. Ambele, C. Dessels, C. Durandt, M. S. Pepper, Genome-wide analysis of gene expression during adipogenesis in human adipose-derived stromal cells reveals novel patterns of gene expression during adipocyte differentiation. *Stem Cell Res.* **16**, 725–734 (2016).
35. H. Hwa Cho, Y. C. Bae, J. S. Jung, Role of toll-like receptors on human adipose-derived stromal cells. *Stem Cells* **24**, 2744–2752 (2006).
36. D. Wu, C. H. Poholek, S. Majumder, Q. Liu, S. K. Revu, K. Mohib, D. M. Rothstein, M. J. McGeachy, IL-17-dependent fibroblastic reticular cell training boosts tissue protective mucosal immunity through IL-10-producing B cells. *Sci. Immunol.* **6**, eaao3669 (2021).
37. P. J. Skene, J. G. Henikoff, S. Henikoff, Targeted in situ genome-wide profiling with high efficiency for low cell numbers. *Nat. Protoc.* **13**, 1006–1019 (2018).
38. M. Bombardieri, F. Barone, D. Lucchesi, S. Nayar, W. B. van den Berg, G. Proctor, C. D. Buckley, C. Pitzalis, Inducible tertiary lymphoid structures, autoimmunity, and exocrine dysfunction in a novel model of salivary gland inflammation in C57BL/6 mice. *J. Immunol.* **189**, 3767–3776 (2012).
39. D. Woetzel, R. Huber, P. Kupfer, D. Pohlers, M. Pfaff, D. Driesch, T. Häupl, D. Koczan, P. Stiehl, R. Guthke, R. W. Kinne, Identification of rheumatoid arthritis and osteoarthritis patients by transcriptome-based rule set generation. *Arthritis Res. Ther.* **16**, R84 (2014).

40. M. B. Buechler, W. Fu, S. J. Turley, Fibroblast-macrophage reciprocal interactions in health, fibrosis, and cancer. *Immunity* **54**, 903–915 (2021).
41. M. G. Connor, T. M. N. Camarasa, E. Patey, O. Rasid, L. Barrio, C. M. Weight, D. P. Miller, R. S. Heyderman, R. J. Lamont, J. Enninga, M. A. Hamon, The histone demethylase KDM6B fine-tunes the host response to *Streptococcus pneumoniae*. *Nat. Microbiol.* **6**, 257–269 (2021).
42. C. Li, E. Lam, C. Perez-Shibayama, L. A. Ward, J. Zhang, D. Lee, A. Nguyen, M. Ahmed, E. Brownlie, K. V. Korneev, O. Rojas, T. Sun, W. Navarre, H. H. He, S. Liao, A. Martin, B. Ludewig, J. L. Gommerman, Early-life programming of mesenteric lymph node stromal cell identity by the lymphotoxin pathway regulates adult mucosal immunity. *Sci. Immunol.* **4**, eaax1027 (2019).
43. J. L. Gregory, A. Walter, Y. O. Alexandre, J. L. Hor, R. Liu, J. Z. Ma, S. Devi, N. Tokuda, Y. Owada, L. K. Mackay, G. K. Smyth, W. R. Heath, S. N. Mueller, Infection programs sustained lymphoid stromal cell responses and shapes lymph node remodeling upon secondary challenge. *Cell Rep.* **18**, 406–418 (2017).
44. I. Korsunsky, K. Wei, M. Pohin, E. Y. Kim, F. Barone, T. Major, E. Taylor, R. Ravindran, S. Kemble, G. F. M. Watts, A. H. Jonsson, Y. Jeong, H. Athar, D. Windell, J. B. Kang, M. Friedrich, J. Turner, S. Nayar, B. A. Fisher, K. Raza, J. L. Marshall, A. P. Croft, T. Tamura, L. M. Sholl, M. Vivero, I. O. Rosas, S. J. Bowman, M. Coles, A. P. Frei, K. Lassen, A. Filer, F. Powrie, C. D. Buckley, M. B. Brenner, S. Raychaudhuri, Cross-tissue, single-cell stromal atlas identifies shared pathological fibroblast phenotypes in four chronic inflammatory diseases. *Med* **3**, 481–518.e14 (2022).
45. A. E. Denton, E. J. Carr, L. P. Magiera, A. J. B. Watts, D. T. Fearon, Embryonic FAP$^+$ lymphoid tissue organizer cells generate the reticular network of adult lymph nodes. *J. Exp. Med.* **216**, 2242–2252 (2019).
46. Q. Chai, L. Onder, E. Scandella, C. Gil-Cruz, C. Perez-Shibayama, J. Cupovic, R. Danuser, T. Sparwasser, S. A. Luther, V. Thiel, T. Rülicke, J. V. Stein, T. Hehlgans, B. Ludewig, Maturation of lymph node fibroblastic reticular cells from myofibroblastic precursors is critical for antiviral immunity. *Immunity* **38**, 1013–1024 (2013).
47. M. Lütge, N. B. Pikor, B. Ludewig, Differentiation and activation of fibroblastic reticular cells. *Immunol. Rev.* **302**, 32–46 (2021).
48. A. Bellomo, I. Mondor, L. Spinelli, M. Lagueyrie, B. J. Stewart, N. Brouilly, B. Malissen, M. R. Clatworthy, M. Bajénoff, Reticular fibroblasts expressing the transcription factor WT1 define a stromal niche that maintains and replenishes splenic red pulp macrophages. *Immunity* **53**, 127–142.e7 (2020).
49. D. C. Dasoveanu, H. J. Park, C. L. Ly, W. D. Shipman, S. Chyou, V. Kumar, D. Tarlinton, B. Ludewig, B. J. Mehrara, T. T. Lu, Lymph node stromal CCL2 limits antibody responses. *Sci. Immunol.* **5**, eaaw0693 (2020).
50. J. Giri, R. Das, E. Nylen, R. Chinnadurai, J. Galipeau, CCL2 and CXCL12 derived from mesenchymal stromal cells cooperatively polarize IL-10$^+$ tissue macrophages to mitigate gut injury. *Cell Rep.* **30**, 1923–1934.e4 (2020).
51. R. Yang, Y. Yao, P. Wang, Hypoxia-induced the upregulation of stromal cell-derived factor 1 in fibroblast-like synoviocytes contributes to migration of monocytes into synovium tissue in rheumatoid arthritis. *Cell Biosci.* **8**, 11 (2018).
52. S. Zou, D. Zhang, Z. Xu, X. Wen, Y. Zhang, JMJD3 promotes the epithelial-mesenchymal transition and migration of glioma cells via the CXCL12/CXCR4 axis. *Oncol. Lett.* **18**, 5930–5940 (2019).
53. J.-J. Wang, X. Wang, Y.-E. Xian, Z.-Q. Chen, Y.-P. Sun, Y.-W. Fu, Z.-K. Wu, P.-X. Li, E.-S. Zhou, Z.-T. Yang, The JMJD3 histone demethylase inhibitor GSK-J1 ameliorates lipopolysaccharide-induced inflammation in a mastitis model. *J. Biol. Chem.* **298**, 102017 (2022).
54. G. Ren, Y. Liu, X. Zhao, J. Zhang, B. Zheng, Z.-R. Yuan, L. Zhang, X. Qu, J. A. Tischfield, C. Shao, Y. Shi, Tumor resident mesenchymal stromal cells endow naïve stromal cells with tumor-promoting properties. *Oncogene* **33**, 4016–4020 (2014).
55. F. Guilloton, G. Caron, C. Ménard, C. Pangault, P. Amé-Thomas, J. Dulong, J. De Vos, D. Rossille, C. Henry, T. Lamy, O. Fouquet, T. Fest, K. Tarte, Mesenchymal stromal cells orchestrate follicular lymphoma cell niche through the CCL2-dependent recruitment and polarization of monocytes. *Blood* **119**, 2556–2567 (2012).
56. M. M. E. de Jong, Z. Kellermayer, N. Papazian, S. Tahri, D. H. Op Bruinink, R. Hoogenboezem, M. A. Sanders, P. C. van de Woestijne, P. K. Bos, C. Khandanpour, J. Vermeulen, P. Moreau, M. van Duin, A. Broijl, P. Sonneveld, T. Cupedo, The multiple myeloma microenvironment is defined by an inflammatory stromal cell landscape. *Nat. Immunol.* **22**, 769–780 (2021).
57. Y. Zhang, L. Shen, D. G. Stupack, N. Bai, J. Xun, G. Ren, J. Han, L. Li, Y. Luo, R. Xiang, X. Tan, JMJD3 promotes survival of diffuse large B-cell lymphoma subtypes via distinct mechanisms. *Oncotarget* **7**, 29387–29399 (2016).
58. R. Mathur, L. Sehgal, O. Havranek, S. Köhrer, T. Khashab, N. Jain, J. A. Burger, S. S. Neelapu, R. E. Davis, F. Samaniego, Inhibition of demethylase KDM6B sensitizes diffuse large B-cell lymphoma to chemotherapeutic drugs. *Haematologica* **102**, 373–380 (2017).
59. N. Bigot, A. Mouche, M. Preti, S. Loisel, M.-L. Renoud, R. Le Guével, L. Sensebé, K. Tarte, R. Pedeux, Hypoxia differentially modulates the genomic stability of clinical-grade ADSCs and BM-MSCs in long-term culture. *Stem Cells* **33**, 3608–3620 (2015).
60. G. Yu, L.-G. Wang, Q.-Y. He, ChIPseeker: An R/Bioconductor package for ChIP peak annotation, comparison and visualization. *Bioinformatics* **31**, 2382–2383 (2015).
61. S. Heinz, C. Benner, N. Spann, E. Bertolino, Y. C. Lin, P. Laslo, J. X. Cheng, C. Murre, H. Singh, C. K. Glass, Simple combinations of lineage-determining transcription factors prime cis-regulatory elements required for macrophage and B cell identities. *Mol. Cell* **38**, 576–589 (2010).
62. H. Han, J.-W. Cho, S. Lee, A. Yun, H. Kim, D. Bae, S. Yang, C. Y. Kim, M. Lee, E. Kim, S. Lee, B. Kang, D. Jeong, Y. Kim, H.-N. Jeon, H. Jung, S. Nam, M. Chung, J.-H. Kim, I. Lee, TRRUST v2: An expanded reference database of human and mouse transcriptional regulatory interactions. *Nucleic Acids Res.* **46**, D380–D386 (2018).

Acknowledgments: Cell sorting was performed at the Biosit Flow Cytometry and Cell Sorting Facility CytomeTRI (UMS 6480 Biosit). High-throughput sequencing was performed by the ICGex NGS platform of the Institut Curie supported by the grants ANR-10-EQPX-03 (Equipex) and ANR-10-INBS-09-08 (France Génomique Consortium) from the ANR ("Investissements d'Avenir" program), by the ITMO-CANCER, and by the SiRIC-Curie program (SiRIC grant INCa-DGOS-4654). We are indebted to the Centre de Ressources Biologiques (CRB)–Santé (BB-0033-00056) of Rennes hospital for its support in the processing of biological samples. We thank C. Tascon (Purification and Analysis of Proteins Core facility, UMR-CNRS 6290) for the production of the pA/G-MNase. **Funding:** This work is supported by the Institut National du cancer (INCA INCA AAP PLBIO-17-06, CALYS and INCA AAP PLBIO-21-197, CAFHeros), the LLS (TRP 6593-20), the Ligue Régionale Contre le Cancer (dept 35 and 44), the Ligue Nationale Contre le Cancer (Equipe Labellisée), and the Infrastructure Program EcellFrance (ANR-11-INSB-005). M.S. is recipient of a doctoral fellowship from the Region Bretagne, the Ligue Régionale (*35*) Contre le Cancer, and the Ligue Nationale Contre le Cancer. N.Ba is recipient of a doctoral fellowship from the Ligue Nationale Contre le Cancer. A.M. is recipient of a postdoctoral fellowship from the Region Bretagne. S.L. was supported by a specific grant from the LabEx IGO program (ANR11-LABX-0016). **Author contributions:** M.S. designed and performed experiments, analyzed data, and contributed to writing. V.S., S.L., and J.S.-V. analyzed data. N.Ba. performed experiments and analyzed data. S.N. and F.B. performed the study on murine TLS. C.M., A.M., M.G., M.L., and F.J. provided technical assistance. L.V. generated data on native ASCs. S.B. and M.B. run the RNA-seq. F.M.-G. provided knowledge on stromal cell commitment. F.M. provided knowledge on LSC and technical assistance. N.Be. provided adipose tissue samples. K.T. designed and supervised research and wrote the paper. D.R. designed and supervised research, performed experiments, analyzed data, and wrote the paper. **Competing interests:** F.M.-G. received research support from Innate-Pharma, Roche, and Bristol-Myers-Squibb (BMS). The other authors declare no competing interests. **Data and materials availability:** All data needed to evaluate the conclusions in the paper are present in the paper and/or the Supplementary Materials. RNA-seq and CUT&RUN data generated during this study are available under GEO accession number GSE180245.

Submitted 24 February 2023
Accepted 27 October 2023
Published 29 November 2023
10.1126/sciadv.adh2708